CO_2 Capture in Dry and Wet Conditions in UTSA-16 Metal-Organic Framework

Alessio Masala[†a,] Jenny G. Vitillo[†a], Giorgia Mondino[b], Carlos A. Grande[*b], Richard Blom[b], Maela Manzoli[c], Marc Marshall[d], and Silvia Bordiga[*a]

[a]Department of Chemistry, NIS and INSTM reference Centres, University of Torino, Via G. Quarello 15/A, 10135 and Via P. Giuria 7, 10125 Torino, Italy.
[b]SINTEF Materials and Chemistry, P.O. Box 124 Blindern, N0314 Oslo, Norway.
[c]Department of Drug Science and Technology, NIS and INSTM reference Centres, University of Torino, Via Giuria 9, 10125 Torino, Italy
[d]School of Chemistry, Monash University, 3800 Victoria, Australia.

†These authors contributed equally to this paper

Corresponding author:
silvia.bordiga@unito.it
carlos.grande@sintef.no

Contents

S1 Preparation of the sample

UTSA-16 was obtained by hydrothermal synthesis as follows: $Co(OAc)_2 \cdot 4H_2O$ (0.249 g, 1 mmol), $C_6H_8O_7 \cdot H_2O$ (0.21 g, 1 mmol), KOH (0.168 g, 3 mmol), H_2O (2.5 ml) and C_2H_5OH (2.5 ml) in the molar ratio 1:1:3:139:43 were put in a Teflon-lined 23 ml Parr acid digestion bomb. The bomb was then placed in a furnace that was heated from room temperature to 393 K in half an hour, kept at 393 K for 2 days, and then slowly cooled to room temperature at a rate of 4 K h^{-1}. All the chemicals used in this synthesis were commercially available and were purchased from Sigma Aldrich.

S2 Volumetric CO₂, N₂ adsorption measurements

The fitting parameters as obtained from Single and Dual-site Langmuir model fit of CO_2 and N_2 isotherms showed in Fig. 1b are reported in Table S1 Table S2, respectively.

Table S1 CO_2 isotherm fitting parameters. Single and Dual-site Langmuir model fit parameters for CO_2 adsorption isotherms of UTSA-16 at 298, 333 and 363 K and 1 bar.

<table>
<tr><td>

T = 298 K:

$$q \equiv q_A + q_B = \frac{q_{sat,A} b_A p}{1 + b_A p} + \frac{q_{sat,B} b_B p}{1 + b_B p}$$

$q_{sat,A} = 5.022 \; mol \; kg^{-1}$

$q_{sat,B} = 0.001 \; mol \; kg^{-1}$

$b_A = 6.43 * 10^{-5} Pa^{-1}$

$b_B = 3.89 * 10^{-11} Pa^{-1}$

</td></tr>
<tr><td>

T = 333 K:

$$q = \frac{q_{sat} b p}{1 + b p}$$

$q_{sat} = 4.776 \; mol \; kg^{-1}$

</td></tr>
</table>

$$b = 1.62 * 10^{-5} Pa^{-1}$$

T = 363 K:

$$q = \frac{q_{sat}bp}{1 + bp}$$

$$q_{sat} = 6.567 \; mol \; kg^{-1}$$

$$b = 3.28 * 10^{-6} Pa^{-1}$$

Table S2 N_2 isotherm fitting parameters. Single-site Langmuir model fit parameters for N_2 adsorption isotherms of UTSA-16 at 298, 333 and 363 K and 1 bar.

T = 298 K:

$$q = \frac{q_{sat}bp}{1 + bp}$$

$$q_{sat} = 3.584 \; mol \; kg^{-1}$$

$$b = 4.75 * 10^{-7} Pa^{-1}$$

T = 333 K:

$$q = \frac{q_{sat}bp}{1 + bp}$$

$$q_{sat} = 4.699 \; mol \; kg^{-1}$$

$$b = 2.14 * 10^{-7} Pa^{-1}$$

T = 363 K:

$$q = \frac{q_{sat}bp}{1 + bp}$$

$$q_{sat} = 1.797 \; mol \; kg^{-1}$$

$$b = 3.72 * 10^{-7} Pa^{-1}$$

CO_2 and N_2 adsorption isotherms of Mg_2(dobdc) (Mg-CPO-27 or Mg-MOF-74) and Cu_3(btc)$_2$ (HKUST-1) reported in Supplementary Figure S1 and Figure S2 have been digitized from the literature and then fitted with a cubic spline.
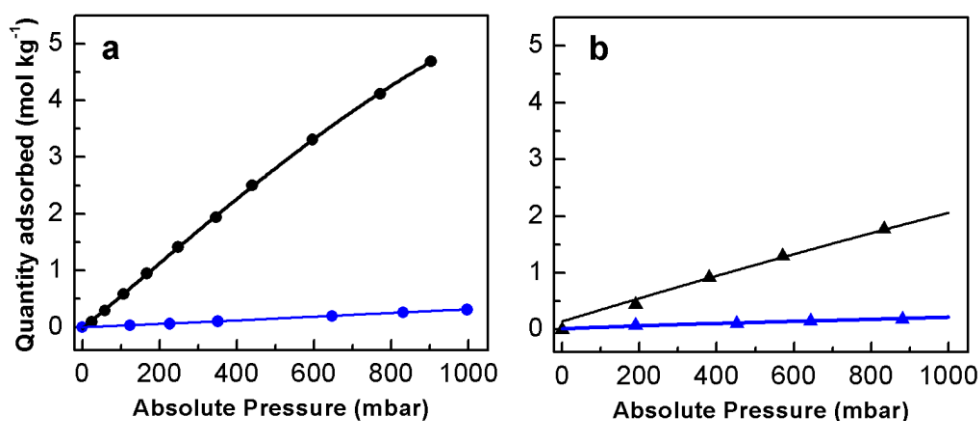
Figure S1 Sorption properties of $Cu_3(btc)_2$. towards CO_2 and N_2. CO_2 and N_2 adsorption isotherms measured at **a,** 295 K (●) by Wang et al.,[1] and at b) 333 K (▲) by Al-Janabi et al.[2] The isotherms are reported up to 1 bar for CO_2 (black) and N_2 (blue). Symbols represent experimental data while continuous lines represent the fitted curves, through cubic spline function.
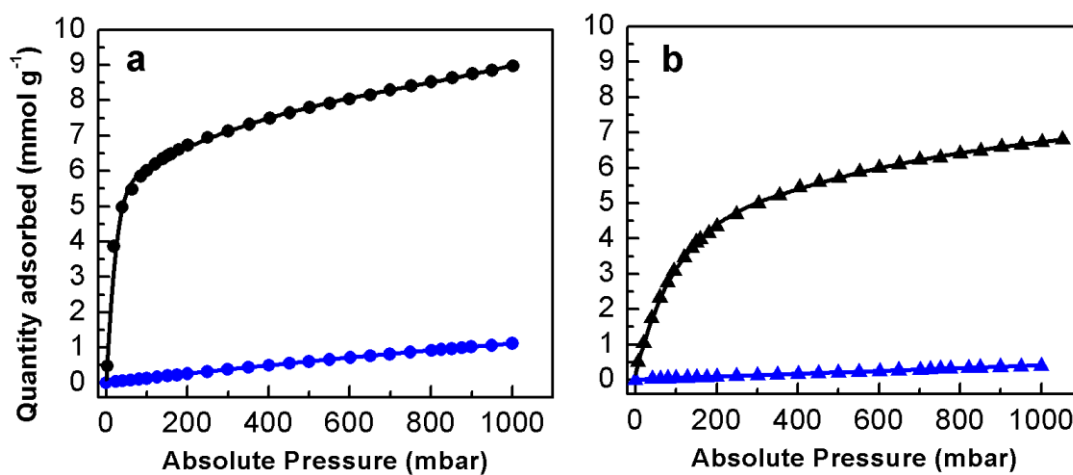

Figure S2 Sorption properties of $Mg_2(dobdc)$ towards CO_2 and N_2. CO_2 and N_2 adsorption isotherms measured at **a,** 293 (●) and **b,** 333 (▲), until 1 bar for CO_2 (black) and N_2 (blue), by Mason et al.[3] Symbols represent experimental data while continuous lines represent the fitted curves, through cubic spline function.

S2.1 CO_2 and N_2 isosteric heat

The isosteric heat q_{st} calculated for CO_2 and N_2 for UTSA-16 is reported in Table S3 along with similar values reported for other MOFs in the literature.

The q_{st} was obtained from the isotherms reported in Fig. 1b by the following procedure: i) The isotherms reported in Fig. 1b were fitted by using the equation reported in Table S1. ii) The $\ln(p/p0)$ is plotted as a function of $1/T$, where p is the pressure and $p0$ is a reference pressure ($p0 = 1$ bar), for each coverage. iii) Each set of points is fitted by a straight line (isosteric curve) whose slope is equal to $-q_{st}/R$, if we assume a Langmuir behaviour of the adsorption and by applying the Clausius-Clapeyron equation. In the case of CO_2 a dual-site Langmuir equation (fitting of isotherms curves reported in Fig. 1b, black symbols) was used. In the case of N_2 single-site Langmuir equations (fitting of isotherms reported in Fig. 1b, blue symbols) were used.

For Mg_2(dobdc), the value reported in Table S3 has been here calculated by fitting of the data reported in ref. [3] (see Figure S2). A graph reporting the dependence of qst of CO_2 and N_2 on the coverage for UTSA-16 is reported in Figure S3. A similar graph for N_2 on Mg_2(dobdc) is reported in Figure S4. All the data reported in the Table are significantly higher than the liquefaction heat of CO_2 (16.7 kJ mol^{-1})[4] and N_2 (5.6 kJ mol^{-1}).[5]

Table S3 CO_2 and N_2 isosteric heat (q_{st}) for different MOFs.

Adsorber	Adsorbate	q_{st} (kJ mol^{-1}) average value	Reference
UTSA-16	CO_2	37	Present work
Cu$_3$(BTC)$_2$	CO_2	27-24	[1-2, 6-7]
Ni$_2$(dobdc)	CO_2	42	[8]
Mg$_2$(dobdc)	CO_2	47-39	[9-11]
UTSA-16	N_2	13	Present work
Cu$_3$(BTC)$_2$	N_2	14.5	[2]
Ni$_2$(dobdc)	N_2	17[*]	[12]
Mg$_2$(dobdc)	N_2	23[**]	Present work

*Value obtained through variable temperature infrared spectroscopy. **Value obtained by applying the procedure described above to the N_2 isotherms at 293 and 333 K of Fig. S2. The complete set of data is reported in Fig. S4.
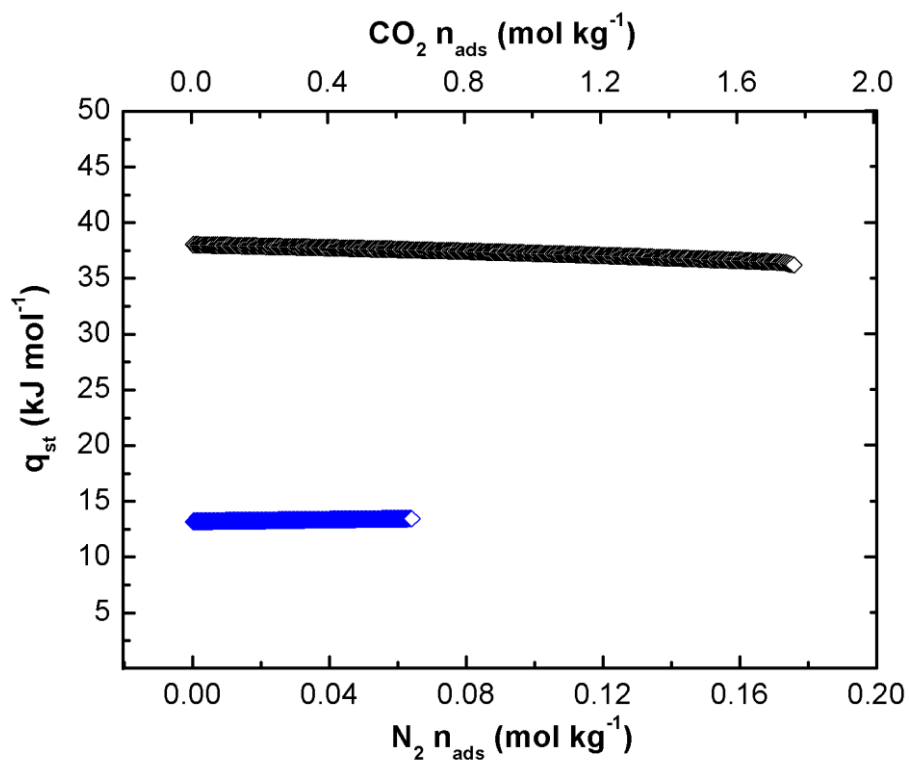
Figure S3 Isosteric heat adsorptions in UTSA-16. q_{st} values of CO_2 (black symbols) and N_2 (blue symbols) as a function of gas loading. Note the different scales in abscissa: top-x refers to CO_2 coverage, down-x refers to N_2 coverage.

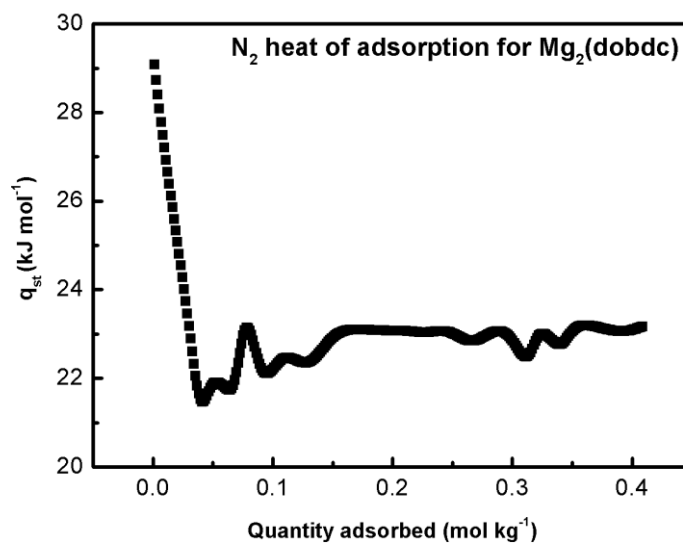**Figure S4** Mg_2(dobdc) isosteric heat of adsorption. q_{st} of N_2 in Mg_2(dobdc) as a function of loading. The trend reported was obtained by applying the procedure above mentioned to the N_2 isotherms (at 293 and 333 K) reported in Figure S2a and Figure S2b.

S2.2   CO$_2$/N$_2$ selectivity

IAST selectivity, as defined by the work of Myers & Prausnitz,[13] has been calculated for CO$_2$/N$_2$ for a 10%CO$_2$/90%N$_2$ flow using the pyIAST software of Simon et al.,[14] following the detailed step procedure reported in the literature.[6] The CO$_2$/N$_2$ selectivities are reported in Table S4 as S_{IAST}. In Table S5, the CO$_2$/N$_2$ selectivities for UTSA-16 were calculated by using equation (1) considering the adsorbed quantities for CO$_2$ and N$_2$ identical in the gas mixture and in a pure gas atmosphere. This has been done in order to allow the comparison with other MOFs reported in the literature.[15]

Table S4 IAST selectivity factors for a CO$_2$:N$_2$ binary gas mixture at 298, 333 and 363 K and 1 bar have been calculated from single component isotherms at CO$_2$: N$_2$ ratio of 10 : 90 % (S_{IAST}).

Temperature (T)	CO$_2$ at 0.10 bar	N$_2$ at 0.90 bar	S_{IAST}
298	1.95	0.15	171
333	0.60	0.09	80
363	0.17	0.06	34

Table S5 Comparison between CO_2/N_2 selectivity factors of different MOFs. This comparison has been done at relevant temperatures and pressure for post-combustion CCUS processes. Partial pressures used are typical of coal-fired power plant exhaust. The selectivity factors have been calculated by approximating the adsorbed quantities for the two adsorbates in the mixture with those measured in the pure-component isotherms (S_{pure}).

	CO_2 at 0.15 bar	N_2 at 0.75 bar	S_{pure}	T (K)	Reference
UTSA-16	2.54	0.12	103	298	Present work
$Cu_3(BTC)_2$	0.84	0.23	18	295	[1, 15]
$Mg_2(dobdc)$	6.41	0.87	37	293	[3, 15]
UTSA-16	0.90	0.07	60	333	Present work
$Cu_3(BTC)_2$	0.45	0.17	13	333	[1, 15]
$Mg_2(dobdc)$	3.88	0.31	61	333	[3, 15]

The digitized data of Supplementary Figure S1 and Figure S2 were used for calculating CO_2/N_2 selectivity factors.

S2.3   TSA and PSA working capacity

TSA working capacity has been evaluated by taking the difference between the quantity adsorbed at the post-combustion adsorption conditions (313 K and CO_2 partial pressure of 0.15 bar) and the quantity desorbed at 393 K and total flue gas pressure of 1 bar.[3] For the calculation of working capacities in $Mg_2(dobdc)$, MOF-177[3] and NaX, we used the isotherms reported by Mason et al.,[3] Cavenati et al.[16] and Belmabkhout et al.[17]
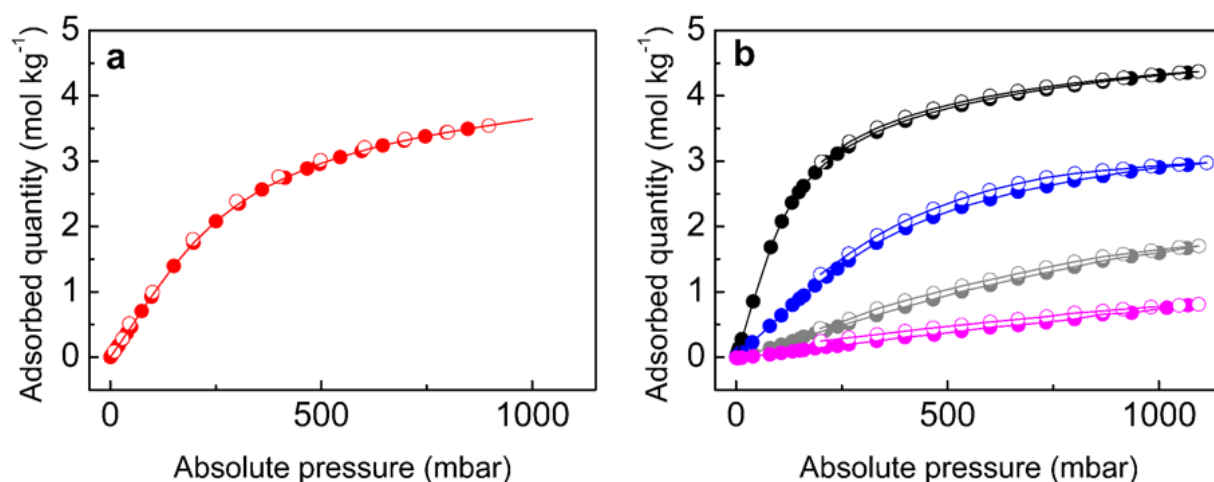
Figure S5   Adsorption and desorption isotherms of CO_2 on UTSA-16 from 0 to 1 bar at a) 313 K (red points), b) 298 (black points), 333 (blue points), 363 (grey points) and 393 K (magenta points). Full symbols refer to the adsorption isotherm; empty symbols refer to desorption isotherm. Bold lines represent the fitting of experimental points.

Table S6   TSA working capacity (WC) of UTSA-16, NaX and $Mg_2(dobdc)$ at adsorption conditions of 313 K and 0.15 bar and desorption condition of 393 K and 1 bar .

Material	*Working capacity (mol kg^{-1})*
UTSA-16	0.62
NaX	0.89
MOF-177	-0.16
$Mg_2(dobdc)$	1.94

PSA working capacity has been instead evaluated by taking the difference between the quantity adsorbed at flue gas pressure and the quantity adsorbed at the lower purge pressure.[15] For the calculation of working capacities in $Mg_2(dobdc)$, we used the isotherms reported by Mason et al.[3]

Table S7   PSA working capacity (WC) of UTSA-16 and Mg$_2$(dobdc) at adsorption temperature of 313 and 333 K.

Material	Total uptake @ 313 K and 1 bar (mol kg^{-1})	Total uptake @ 333 K and 1 bar (mol kg^{-1})	WC @ 313 K (mol kg^{-1})	WC @ 333 K (mol kg^{-1})
UTSA-16	3.65	2.90	2.2	2.0
Mg$_2$(dobdc)	7.68[3]	6.72	2.3	2.8

S3 UTSA-16 diffusion with pulse and breakthrough measurements

Diffusion measurements were performed on UTSA-16 for CO_2 and N_2 at 298, 333, 363 and 393 K. While pulse chromatography was used to measure diffusion of N_2, diluted breakthrough experiments were instead preferred for CO_2, due to the strongly non-symmetric shape of the CO_2 peaks (due to the high non-linearity of the CO_2 isotherms even at very low pressures). The experimental curves were simulated by using the mathematical model described in section S3.1 in order to obtain the reciprocal diffusion time constant and the Henry constant.

S3.1 Modeling gas diffusion from pulse and breakthrough measurements

The mathematical model used to simulate pulses and breakthrough curves is based on the assumptions of isothermal conditions, linear adsorption isotherm and constant gas velocity. Such assumptions are justified by the low adsorbate concentration compared to the inert gas concentration employed in the experiments. Assuming an axial dispersed plug flow, the mass balance in a differential element of the bed is given by Ruthven et al.:[18]

$$\varepsilon \frac{\partial c}{\partial t} + (1 - \varepsilon)\rho_p \frac{\partial \bar{q}}{\partial t} = \varepsilon D_z \frac{\partial^2 c}{\partial z^2} - u \frac{\partial c}{\partial z} \qquad (S1)$$

Where C is the concentration of adsorbate in the gas phase, ε is the bed void fraction, ρ_p is the pellets density, u is the superficial gas velocity, D_z is the axial dispersion coefficient, and $\bar{q}$ is the averaged amount adsorbed in the pellet. The last is calculated as follows:

$$\bar{q} = \frac{2}{R^3} \int_0^R q r^2 \, dr \qquad (S2)$$

where R is the pellet radius and q is the adsorbed concentration per unit mass of adsorbent, which is obtained from the Fickian description of adsorbate diffusion inside the pellets:

$$\frac{\partial q}{\partial t} = \frac{1}{R^2} \frac{\partial q}{\partial r} \left(D_c r^2 \frac{\partial q}{\partial r} \right) \qquad (S3)$$

At the pellet surface, the adsorbed amount is assumed in equilibrium with the surrounding gas. Therefore, the following boundary conditions are applied to the previous differential equation:

$$q|_{r=R} = q^* \qquad (S4)$$

$$\left. \frac{\partial q}{\partial r} \right|_{r=0} = 0; \qquad (S5)$$

Where the amount adsorbed at the pellet surface, q^*, is calculated with the Henry's law:

$$q^* = KC \qquad (S6)$$

K being the adsorption equilibrium constant.

The axial dispersion coefficient appearing in the mass balance equation was calculated by employing the following correlation:[19]

$$D_z = (0.45 + 0.55\,\varepsilon)D_m + 0.35R\,u \qquad (S7)$$

Where D_m is the molecular diffusivity of the gas.

The model was solved numerically by gPROMS (PSE Enterprise, United Kingdom), employing centered finite differences (CFDM) for discretization of the spatial domains.

Nomenclature

C Molar concentration of adsorbate in gas phase (mol/m^3)

D_z Axial dispersion coefficient (m^2 s^{-1})

D_m Molecular diffusivity of the gas (m^2 s^{-1})

D_c Diffusivity constant

K Henry's law constant (m^3 kg^{-1})

$\bar{q}$ Pellet averaged adsorbed concentration (mol kg^{-1})

q^* Adsorbed concentration in equilibrium with C (mol kg^{-1})

r Adsorbent pellets coordinate (m)

R Adsorbent pellets radius (m)

u Superficial gas velocity (m s^{-1})

z Axial coordinate (m)

ε Bed void fraction

ρ_ρ Pellet density (kg m^{-3})

S3.2   CO$_2$ breakthrough and N$_2$ pulsed chromatography measurements

The experimental parameters characterizing the apparatus used for the CO$_2$ breakthrough measurements are reported in Table S8.

Table S8 Breakthrough experiment parameters. Experimental conditions for breakthrough experiments of CO_2 on UTSA-16.

Bed length	L	cm	7.738
Bed diameter		cm	0.685
Pellet diameter	r	mm	0.2-0.5
Microcrystals diameter**		nm	100-200
Adsorbent mass	m	g	1.601
Pure He flow rate* (for desorption)		ml/min	20
Feed gas flow rate* (for breakthrough)		ml/min	20
CO_2 concentration in feed gas	C_{feed}	%	0.5
Pressure	p	bar	1
Temperatures	T	K	298-333-363-393
Bed void fraction	ε_c		0.34

*measured at room temperature and atmospheric pressure; ** measured by HR-TEM, Figures S15

By measuring the breakthrough curves using a very low gas concentration (Table S8) we are ensuring that the adsorption equilibrium will not have any effect on the diffusion rate and the thermal effects are also minimized allowing to assume that the temperature is constant in the adsorbent. The experimental curves were fitted for each temperature on the basis of the mathematical models described in Section 3.1, by varying the value of diffusion constant (D_c) as exemplified in Figure S6 for the curve at 333 K.
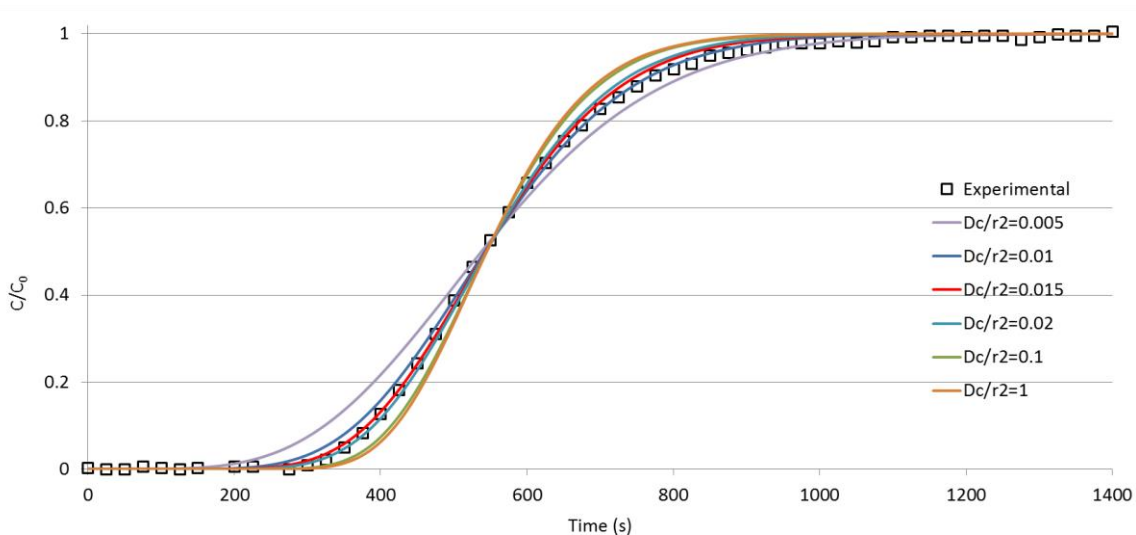
Figure S6 CO_2 breakthrough curves at 333 K. Experimental data ($\square$) compared to model data (solid lines) obtained by using different D_c/r_c^2 values. D_c/r_c^2 values are reported in s^{-1}.

The complete set of CO_2 breakthrough curves and the corresponding modeled curves are shown in Figure S7.
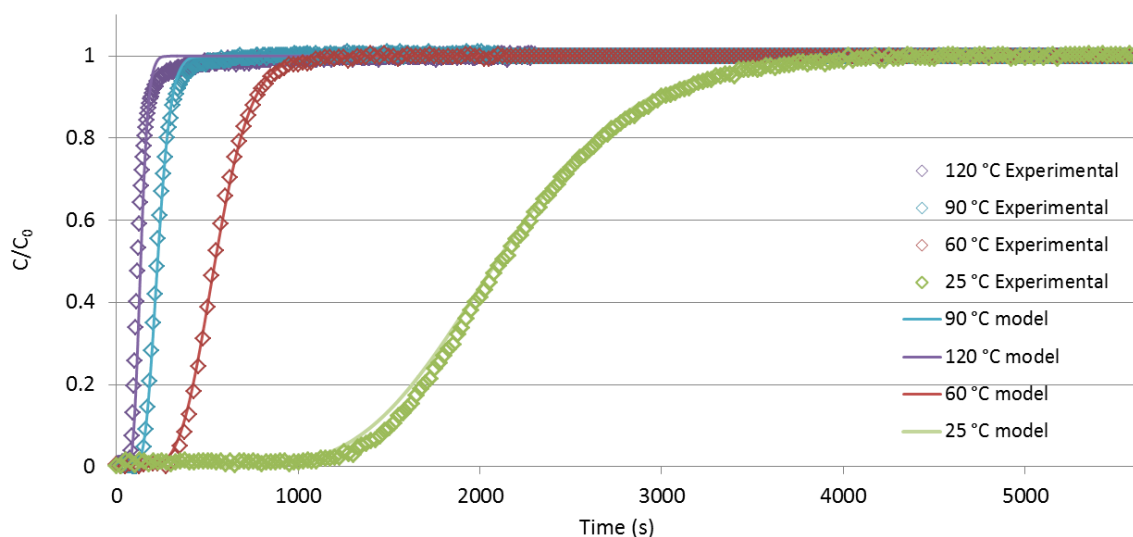

Figure S7 CO_2 breakthrough curves. CO_2 breakthrough curves on UTSA-16 at 298 (green), 333 (red), 363 (blue) and 393 K (violet). Experimental data are represented by diamonds ($\blacklozenge$), model data are represented by solid lines.

The curves relative to the N_2 pulse chromatography measurements at different temperatures and flow rates are reported in Figure S8.
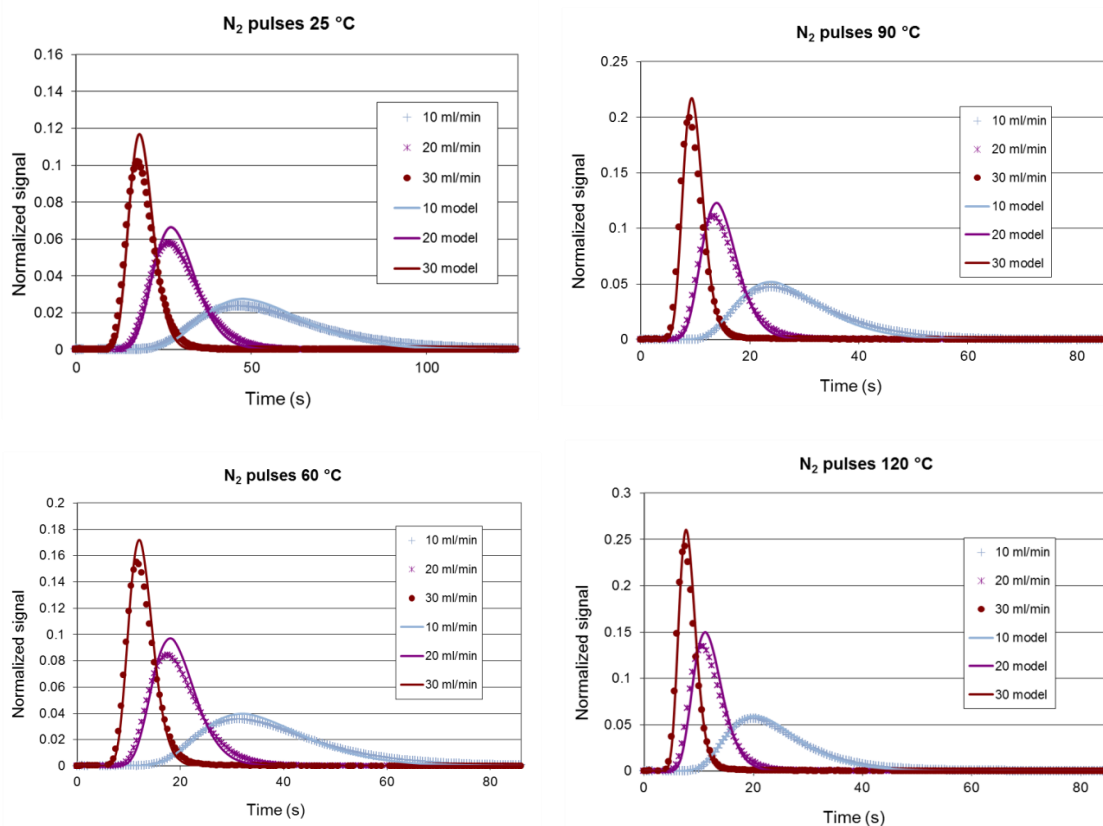

Figure S8 N_2 pulsed chromatographic experiments. Experimental (scatters) and model (continuous lines) curves for N_2 pulse experiments on UTSA-16 at different temperatures (298, 333, 363, 396 K) and different flow rates.

As demonstrated in Figure S8, N_2 diffusion was very fast, indicating a poor affinity towards UTSA-16, at all tested temperatures.

S3.2.1 Henry's law constants

The dimensionless Henry coefficients (K_H) relative to CO_2 adsorption on UTSA-16 were evaluated from the stoichiometric breakthrough time (τ_{st}), using equation (S1):

$$\tau_{st} = \int_0^\infty \left(1 - \frac{C}{C_{feed}}\right) dt = \frac{L}{u}\left[1 + \frac{1-\varepsilon_c}{\varepsilon_c} K_H\right] \tag{S8}$$

Where C is the concentration of adsorbate in the gas phase at the exit of the column, C_{feed} is the concentration of CO_2 in the feed (0.5% CO_2 in He), ε_c is the bed void fraction (0.34), L is the length of the bed, u is the interstitial velocity and K_H is the Henry constant.

Table S8 and Table S9give the parameters used to obtain K_H for CO_2. K_H are reported in Figure S9 against 1/T.

Table S9 CO_2 Henry Constant coefficients. Dimensionless Henry's law constants K_H, stoichiometric breakthrough time (τ_{st}) and interstitial velocity (u) relative to CO_2 breakthrough measurements at different temperatures.

T (K)	1/T (K⁻¹)	*Interstitial velocity u (m s⁻¹)*	τ_{st} (s)	K_H
298.15	0.003354016	0.026899326	2184	390.5666
333.15	0.003001651	0.030057053	566	112.6136
363.15	0.002753683	0.032763675	234	50.60372
393.15	0.002543558	0.037243812	144	35.18218

The dimensionless Henry coefficients (K_H) relative to N_2 adsorption on UTSA-16, were evaluated from the first moment of the pulse as:

$$\mu = \frac{L}{u}\left[1 + \left(\frac{1-\varepsilon_c}{\varepsilon_c}\right)K_H\right] \tag{S9}$$

Where ε_C is the bed void fraction, L is the length of the bed, u is the interstitial velocity and K_H is the Henry constant. Table S8 and Table S10 give the parameters used to obtain K_H for N_2. They are plotted as function of 1/T in Figure S9.

Table S10 N$_2$ Henry Constant coefficients. Dimensionless Henry's law constants K$_H$, stoichiometric breakthrough time (τ_{st}) and interstitial velocity (u) relative to N$_2$ breakthrough measurements at different temperatures and at different flow rates.

| T (K)	1/T (K^{-1})	*Interstitial velocity u (m s^{-1})*	Flux (ml min^{-1})	*K$_H$*
298.15	0.003354016	0.0134497	10	4.54577
298.15	0.003354016	0.0268993	20	4.780998
298.15	0.003354016	0.040349	30	4.637696
333.15	0.003001651	0.0150285	10	3.312335
333.15	0.003001651	0.0300571	20	3.437599
333.15	0.003001651	0.0450856	30	3.323544
363.15	0.002753683	0.0163818	10	2.628248
363.15	0.002753683	0.0327637	20	2.82891
363.15	0.002753683	0.0491455	30	2.752152
393.15	0.002543558	0.0177351	10	2.414638
393.15	0.002543558	0.0354703	20	2.404297
393.15	0.002543558	0.0532054	30	2.392551
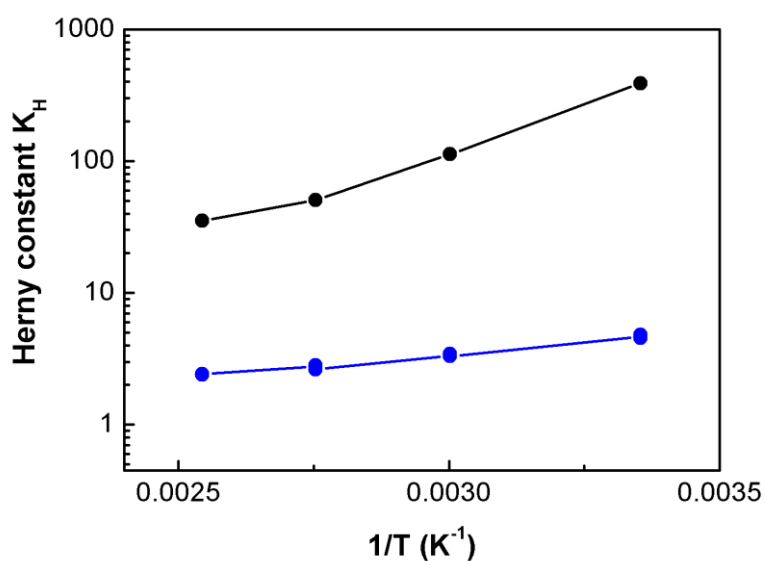
Figure S9 Comparison between CO_2 and N_2 Henry constants. K_H values plotted against 1/T for CO_2 (black) and for N_2 (blue).

It is evident that the Henry's law constants of both N_2 and CO_2 are decreasing with the increasing of the temperature, as expected. K_H for CO_2 are at least one order of magnitude higher than those of N_2, testifying the higher affinity of UTSA-16 to CO_2 with respect to N_2.

The reciprocal diffusion time constant D_c/r_c^2 (expressed in s^{-1}) was obtained by simulating the pulsed peaks and breakthrough curves by using equation (S3):

$$\frac{D_C}{r_C^2} = \frac{D_C^0}{r_C^2} exp\left(-\frac{E_a}{R_g T}\right) \tag{S10}$$

where D_c^0/r_c^2 is the reciprocal diffusion time constant at infinite temperature (in s^{-1}), E_a is the activation energy (kJ mol^{-1}), R_g is the universal gas constant (kJ mol^{-1} K^{-1}), and T is the temperature. The complete set of data is reported in Table S11.

Table S11 Diffusion measurements outputs. Results of the analysis of the diffusion measurements on UTSA-16.

Gas	T (K)	$D_c\ r_c^{-2}$ (s^{-1})	$D_c^0\ r_c^{-2}$ (s^{-1})	E_a kJ (kg^{-1} K^{-1})
CO$_2$	298	0.0025		
	333	0.015	14625	38.42
	363	0.05		
	393	0.1		
N$_2$	298	1		
	333	5	300	11.0
	363	5		
	393	5		

These set of data indicate that diffusion of both gases in UTSA-16 is very fast. It is interesting to notice that the reciprocal diffusivity time constants for CO$_2$ are higher than for the benchmark material 13X zeolite (0.00044 s^{-1} at 323 K).[20] The fast diffusion of CO$_2$ in UTSA-16 is an important feature in view of an employment of this material for real applications.

S4 H$_2$O gravimetric adsorptions and isosteric heat of water adsorption

Water isotherms were obtained for UTSA-16 at 328 and 342 K until 40 mbar and are reported in Figure S10.
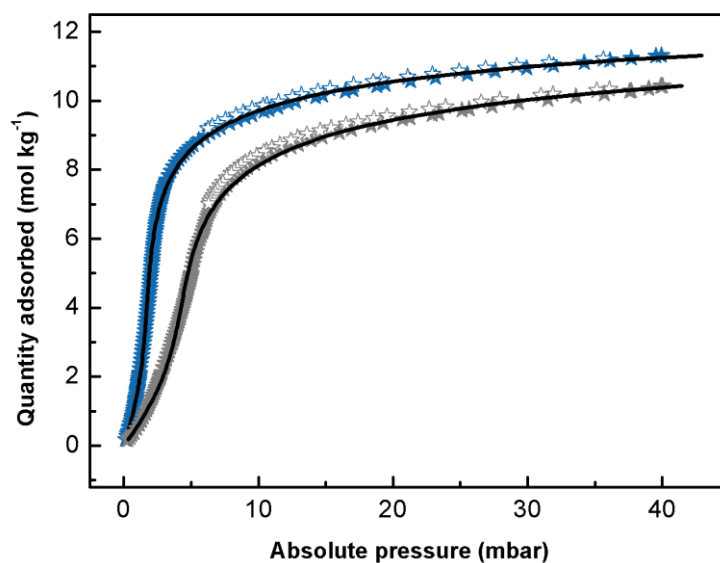
Figure S10 H_2O gravimetric adsorption isotherms on UTSA-16. Experimental H_2O gravimetric isotherms on UTSA-16 at 328 (light blue) and 342 K (grey). Adsorption (full ★) and desorption (empty ☆) branches are reported. Fitted data (black lines) were obtained through a virial-type fitting.

Isotherms of Figure S10 were fitted with a virial-type equation:

$$lnp = lnN + \left(\frac{1}{T}\right) \sum_{i=0}^{m} a_i N^i \qquad (S11)$$

Here p is the pressure expressed in Pa, N is the amount adsorbed in mol kg^{-1}, T is the temperature in K, a_i is the virial coefficient and *m* represents the number of coefficients required to describe the isotherms. The parameters resulting from the fitting are reported in Table S12.

Table S12 | H₂O virial-model fitting parameters. Virial-model fit parameters for water vapour adsorption isotherms on UTSA-16 at 328 and 342 K and 25% relative vapour pressure. K_H represents the Henry constant at temperature T.

T = 328 K:

$$lnp = lnN + \left(\frac{1}{T}\right)\sum_{i=0}^{m} a_i N^i$$

$a_0 = -0.0861$

$a_1 = -0.03829$

$a_2 = 0.00513$

$K_S = 12.51 \, Pa \, kg \, mol^{-1}$

$K_H = 8.00 * 10^{-5} \, mol \, kg^{-1} Pa^{-1}$

T = 342 K:

$$lnp = lnN + \left(\frac{1}{T}\right)\sum_{i=0}^{m} a_i N^i$$

$a_0 = -0.06913$

$a_1 = -0.03796$

$a_2 = 0.00494$

$$K_S = 5.344457 \, Pa \, kg \, mol^{-1}$$

$$K_H = 1.87 * 10^{-4} \, mol \, kg^{-1} Pa^{-1}$$

The kinetics of adsorption of water at 313 K and 40 mbar vapour pressure is reported in Figure S11. After equilibration, the fully desorption of water in presence of dynamic vacuum ($< 1 \, 10^{-3}$ mbar) is obtained after only two hours at 313 K. The fully reversibility of water adsorption at a such low temperature is an unique property among MOFs with open metal sites.
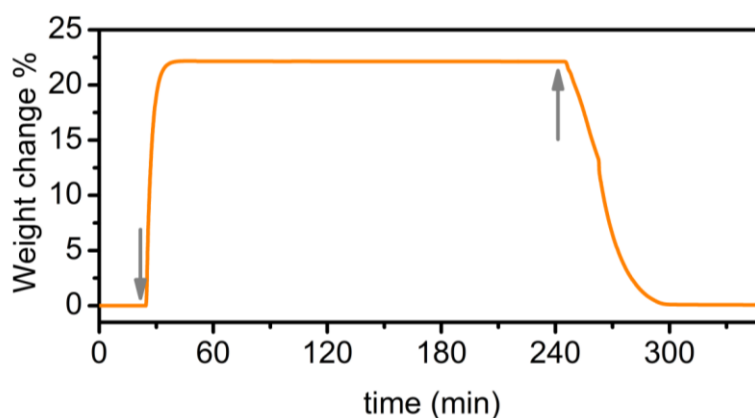

Figure S11 Kinetics of water adsorption on UTSA-16 at 313 K. The material activated at 363 K overnight was contacted with 40 mbar of H_2O until equilibrium was reached and then degassed in dynamic vacuum ($p < 1 \times 10^{-3}$ mbar). All the water was removed in less than 2 h. The up and down arrows mark the starting of the water vapour dosage and the degassing, respectively.

Buoyancy effects were found to affect the weight to less than 0.25% in the pressure and temperature range considered and for that reason negligible. The measured weights were affected by an absolute error lower than 0.01 mg in the conditions adopted (starting sample weight of about 20 mg), corresponding to an error in the calculated mass loss comprised in the range 0.06-0.016 mass%. The skeletal density used in the buoyancy calculations was extracted from Ref. [21].

S5 UTSA-16 structural stability upon wetting

Five CO_2 adsorption desorption cycles were carried out at 298 K, while two adsorption/desorption cycles were carried out at 333, 363 and 393 K respectively, as reported in Table S13 below. A series of corrections has been taken into account: H_2O adsorption isotherms were run between two CO_2 adsorption isotherms to investigate whether there were any changes in CO_2 adsorption capacity following adsorption of H_2O to successively increasing pressures at 298 K and then at following adsorption of H_2O to a pressure of 40 mbar at 333, 363 and 393 K. Pressure values have been corrected for zero error and the known difference between the true pressure and the transducer pressure. A correction for the error resulting from the change in convection currents when gas is introduced into the IGA previously under vacuum has also been made. Both CO_2 and H_2O experimental data of Fig. 4,b (main text) and Figure S12 were fitted with a cubic spline function.

The experiment was done following the sequence:

1) CO_2 adsorption at a specific temperature (full black symbols); 2) CO_2 desorption in high vacuum (not shown); 3) H_2O adsorption until vapor pressure saturation (see the complete set of water isotherm data reported in Fig. S12); 4) H_2O desorption in high vacuum at 363 K; 5) CO_2 adsorption at the same temperature (empty light blue symbols and lines). The desorption temperature of 363 K was adopted in order to allow a faster water removal than at 343 K although the results for the two activation temperatures are fully comparable as demonstrated above. Before these cycles, a test to demonstrate the chemical stability of UTSA-16 towards water, was conducted by carrying out the sequence: 1) CO_2 adsorption to 5 bar at 298 K; 2) H_2O isotherm to 30% relative vapor pressure at 298 K; 3) repetition of steps (1) and (2), but with the H_2O isotherm to 60% relative vapor pressure; 4) repetition of steps (1) and (2), but with the H_2O isotherm to 95% relative vapor pressure; 5) CO_2 isotherm to 5 bar at 298 K; 6) evacuation at 363 K; (7) Repetition of (5); this isotherm is reported with diamond symbols (grey line) in Fig. 4,a of the main text. The gradual increase in final H_2O pressure for the

H_2O isotherms was designed to find the highest water vapour pressure at which the MOF was stable, in the sense that its original CO_2 adsorption capacity was retained.
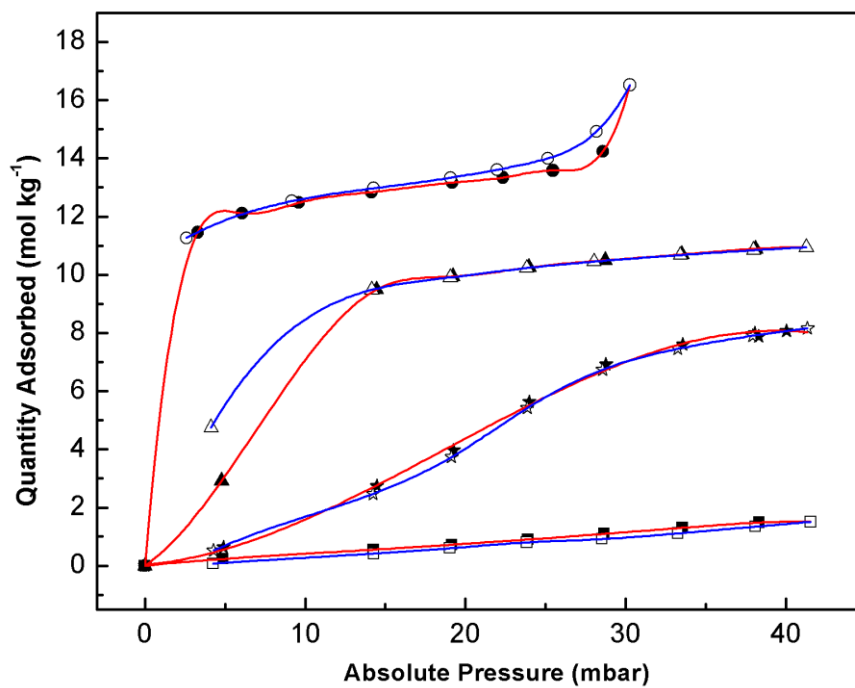

Figure S12 H_2O gravimetric adsorption isotherms on UTSA-16, till > 5 bar. Experimental H_2O gravimetric isotherms on UTSA-16 at 298 (●), 333 (▲), 363 (★) and 393 K (■). Full symbols refer to adsorption experimental data while empty symbols refer to desorption experimental data.

Table S13 CO_2 adsorption uptakes for UTSA-16 in the over-atmosphere pressure range. Each value reported in the Table was obtained by following the procedure explained above in this Supplementary section.

T (K)	*Pre-wetting* n_{ads} (mol g⁻¹)	n_{ads} 1st cycle (mol g⁻¹)	n_{ads} 2nd cycle (mol g⁻¹)	n_{ads} 3rd cycle (mol g⁻¹)	n_{ads} 4th cycle (mol g⁻¹)	n_{ads} 5th cycle (mol g⁻¹)
298	5.22	5.16	5.19	5.06	5.07	4.96
333	4.29	4.31	---	---	---	---
363	3.61	3.58	---	---	---	---
393	2.55	2.64	---	---	---	---

S6 UTSA-16 structural stability upon cycling

Temperature swing adsorption (TSA) cycling experiments were performed on UTSA-16 powder which was pressed into pellets of 0.2 – 0.5 mm size, in order to avoid high pressure drops within the fixed bed.[22]

In order to check the stability of UTSA-16 in terms of CO_2 capacity, a multi-cycle stability test has been done in the presence of water vapour. To perform a meaningful TSA experiment, the adsorbed CO_2 and water must be completely removed in the second part of each cycle; if some CO_2 or water remains adsorbed after a cycle, the loading in the next cycle will be reduced.

A scheme of the experimental setup is reproduced below:
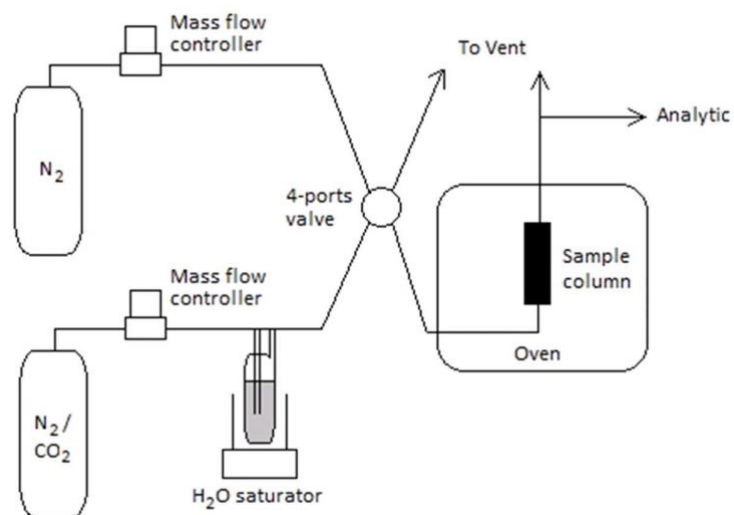
Scheme S1 Stability tests in the presence of moisture. Experimental setup used for cyclic stability tests on MOF materials, in presence of water vapor.

The output signal was analyzed by a thermo conductivity detector (TCD) and a mass spectrometer.

Table S14 Stability tests in the presence of moisture. Experimental parameters used for cyclic stability test on UTSA-16 in presence of water.

Feed Gas	Step time (min)	Temperature set point (K)
CO_2 mix*	7	313
N_2	16	Heating ramp
N_2	10	393 K
N_2	16	Cooling ramp
N_2	15	313 K

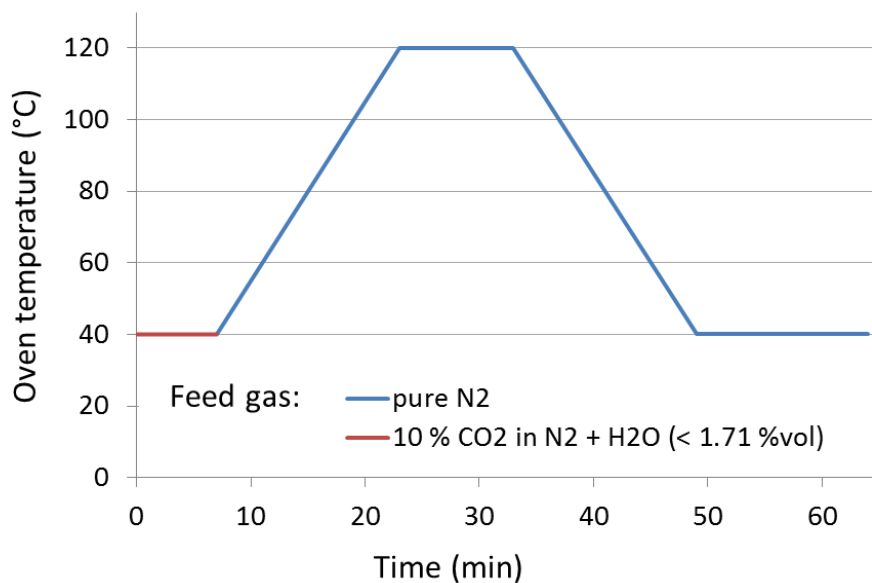* 10 % CO_2/N_2 + H_2O (< 1.71 % vol)

Figure S13 Temperature profile during an adsorption/desorption cycle. The experiments begins with 10% CO_2 in N_2 + H_2O (< 1.71 %vol) composition of the feed gas (red line). When heating is turned on, feed gas is switched to pure N_2.

Both gas streams were kept at constant flow rates of 30 ml/min (value measured at ambient pressure and temperature). The four-ports switching valve, directing the gases either to the adsorbent sample or to the exhaust system, was programmed to perform several cycles in a sequence. The experiment was interrupted after 160 cycles.

The adsorption capacity of UTSA-16 and its stability were also tested by using a dry flow having a composition of 10 % CO_2/N_2. For this experiment, a NETZSCH STA 449 F1 thermo-gravimeter (TG) connected with a QSM 403 C mass spectrometer was used. In this case, a TG was introduced in the setup because the adsorption of CO_2 could be directly measured by the mass difference after the adsorption step (Step 1) and the desorption step (Step 4). The following 5 step-cycle was used:

Step 1: 10 % CO_2/N_2 gas stream (30 ml/min) at 313 K for 7 minutes.

Step 2: Switch to a stream of pure nitrogen while increasing the sample temperature from 313 to 393 K with a heating rate of 5 K/min. Total step length 16 minutes.

Step 3: Purge with pure N_2, at the sample temperature of 393 K for a period of 10 min.

Step 4: Reduce the temperature of the sample to 313 K at a controlled rate of 5 K min^{-1} maintaining a flow of nitrogen. Step length 16 min.

Step 5: Maintain the oven temperature at 313 K for 15 min under a flow of nitrogen. This step was performed to ensure constant temperature in the adsorbent before a new cycle starts.

The TG traces are shown in Figure S14 below. As seen, the cyclic capacity is quite stable over the whole experiment with an estimated average cyclic capacity of 5.7 wt% (1.3 mol kg^{-1}).
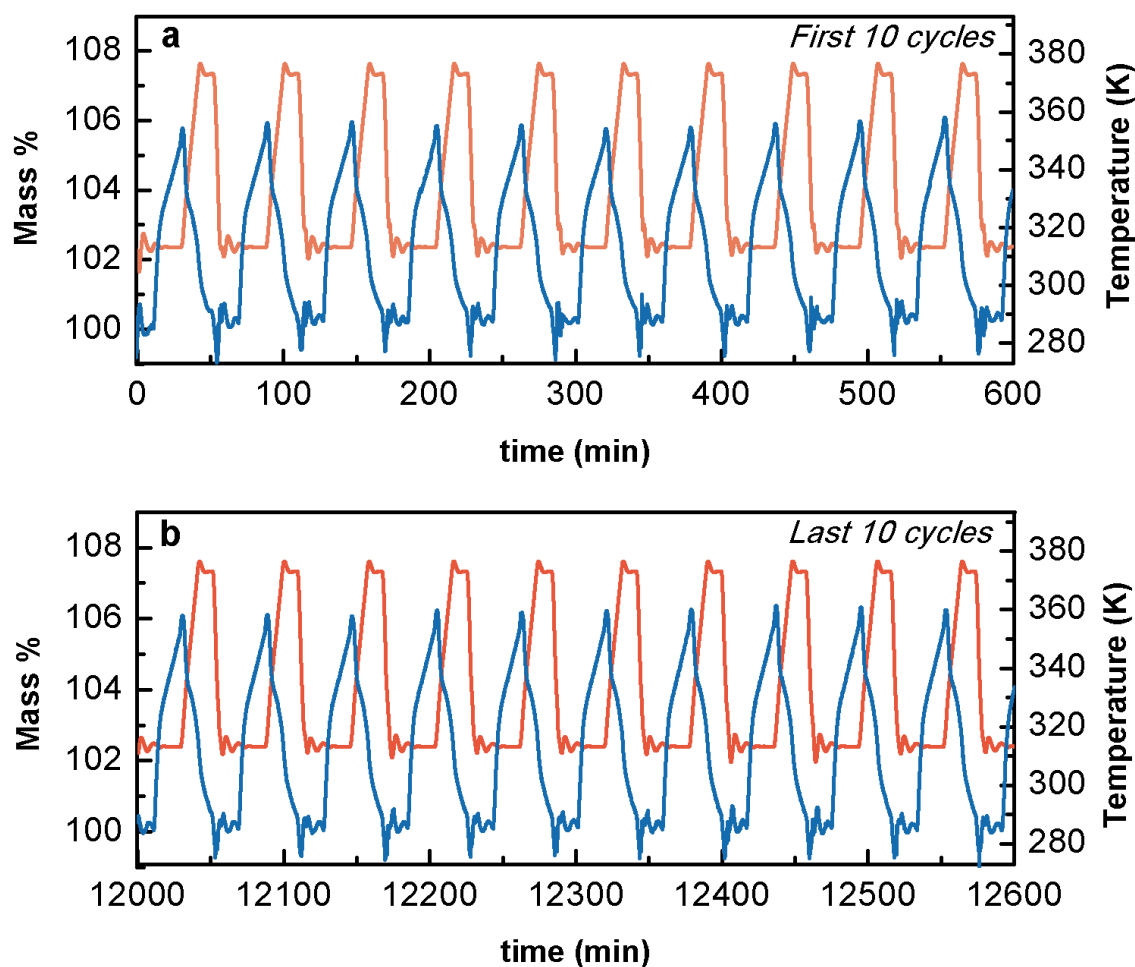

Figure S14 Stability tests in dry conditions. The TG trace during **a,** the first ten and **b,** the last ten cycles of adsorption/desorption of a 10% CO_2/N_2 gas mixture on UTSA-16. The blue line corresponds to CO_2 while the red line corresponds to the temperature.

At the end of the 160 cycles in the wet flow (9.83% CO_2, 88.46% N_2, 1.71% H_2O), the sample was thoroughly characterized by means of a multi-technique approach including powder x-ray diffraction (P-XRD), high resolution transmission electron microscopy (HR-TEM), N_2 and CO_2 volumetry. For comparison, the same analysis was conducted on a fresh UTSA-16 powder.

S6.1   P-XRD

Powder X-Ray Diffraction (P-XRD) technique was used to compare the crystallinity of the samples before and after cycling. P-XRD patterns were collected using a laboratory diffractometer (Panalytical X'Pert Pro Multipurpose Diffractometer) with nickel filter and copper source in Debye-Scherrer geometry. Samples were put in 0.8 mm borosilicate capillaries sealed in N_2 atmosphere and measured in a 2θ range of 2°−102° (scanning step of 0.016° and 0.010° s^{-1}). Capillaries were constantly rotating to avoid effects due to eventual preferential orientations of crystallites.

Figure S15 shows the P-XRD on a fresh (red line) and on the cycled UTSA-16 sample (blue line).
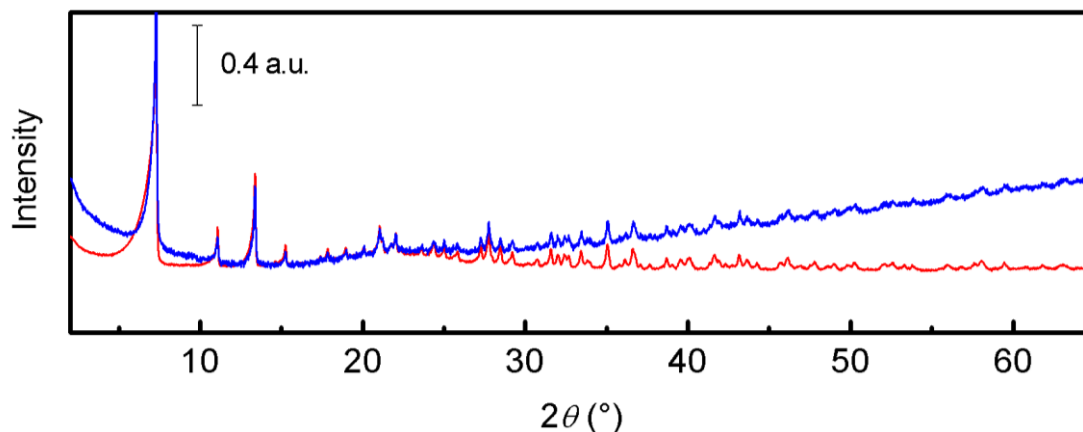
Figure S15 Crystallinity of UTSA-16 after cycling. P-XRD pattern on activated sample of fresh (red line) and cycled UTSA-16 (blue line). Data on the y-axis are expressed in logarithm scale.

A small decrease of the peak intensity was observed after cycling in the 5-10 ° range. This behavior indicates a slight damaging on the material after cycling.

S6.2   HR-TEM

High Resolution Transmission Electron Microscopy (HR-TEM) measurements have been performed on the cycled UTSA-16 sample. The analysis was done by means of a JEOL JEM 3010-UHR microscope operating at 300 kV, equipped with a (2k × 2k)-pixel Gatan US1000 CCD camera. The powdered sample was deposited on a copper grid covered with a lacey carbon film. Images were acquired in a magnification range of 5000X to 150000X to examine the stability of UTSA-16 material under the electron beam. The samples were previously activated overnight (under high vacuum at 363 K) and left in prechamber for 2 hours. In this way, the samples were admitted to the analysis chamber in a very high vacuum condition, allowing us the possibility to collect images avoiding problems related to the release of moisture/solvent in the column of the microscope.
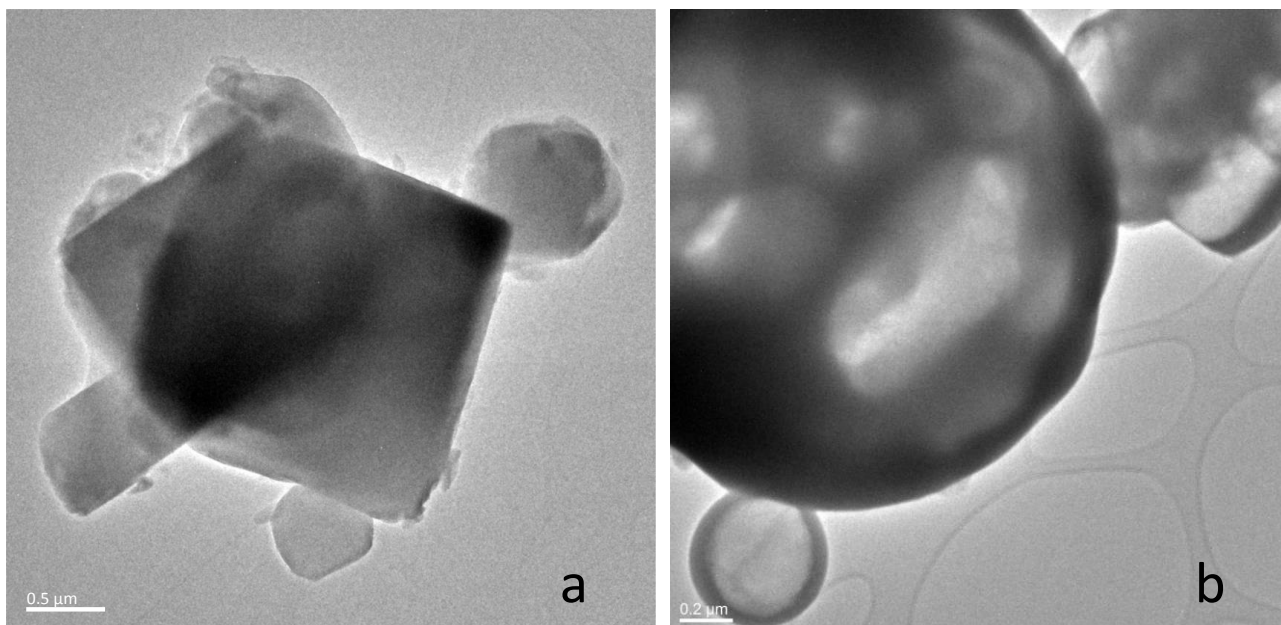
Figure S16 Morphology of UTSA-16 particles. TEM image of cycled UTSA-16 **a,** before and. **b,** after prolonged exposition under the electron beam. Instrumental magnification: 5000X and 10000X, respectively.

Figure S16 illustrates the effect of the electronic beam on activated powder UTSA-16 (part a). The images show that irradiation at high magnification induces the deterioration of the material into rounded shapes not observed at lower magnification, after short time of exposition under the electron beam (part b).
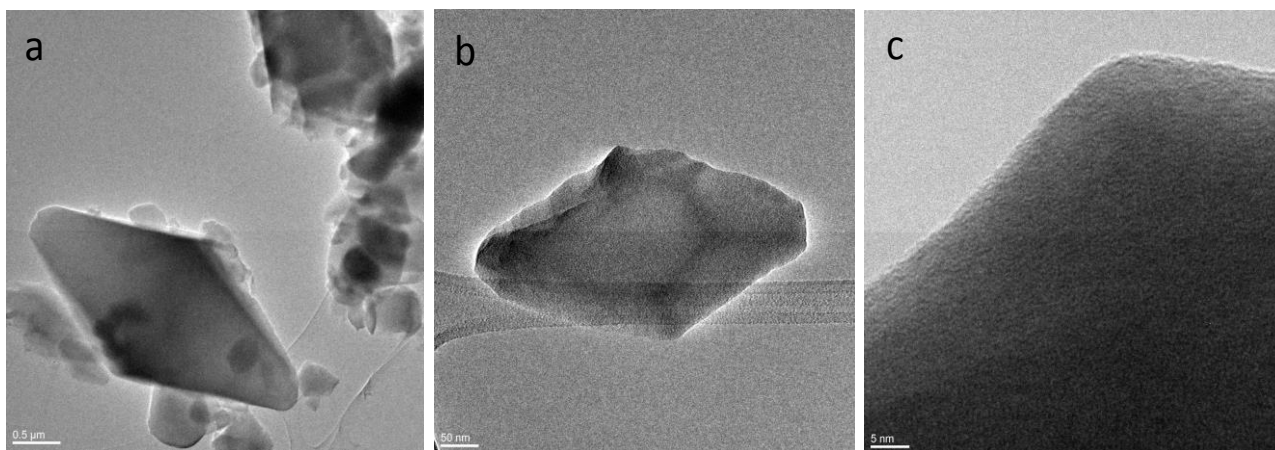
Figure S17 Morphology of UTSA-16 particles after cycling. **a,** and **b,** TEM images of cycled UTSA-16 taken at different magnification. **c,** shows a zoom of (b). Instrumental magnification: 5000X, 40000X and 400000X.

Figure S17 shows the TEM images collected on the cycled UTSA-16 at increasing magnification. It is worth noting that damaging of the sample arises when exposing the material under the electron beam for prolonged time at high magnification (150000-400000X). This phenomenon is considerably delayed if compared to the powder UTSA-16. For what concerns the morphology the images are identical to those previously reported for a fresh UTSA-16 sample.[23]

S6.3   Surface area and volume of the pores

Volumetric N_2 adsorption at 77 K were carried out by means of a Micromeritics ASAP 2020 sorption analyzer on activated UTSA-16 samples (fresh and cycled) to evaluate the surface area and total pore volume. The Langmuir adsorption model was chosen to calculate the surface area of microporous UTSA-16, while the total pore volume was extrapolated from the N_2 adsorption isotherm at $p/p^0 = 0.97$ and multiplied by the N_2 density conversion factor (0.0015468) in order to obtain a value in cm^3 g^{-1} from cc(STP) g^{-1}.

Table S15 Structural features of UTSA-16 particles after cycling. Langmuir surface area and pore's volume of UTSA-16.

	UTSA-16 before cycling	UTSA-16 after cycling
Langmuir surface area ($m^2 \ g^{-1}$)	904	785
Volume of pores ($cm^3 \ g^{-1}$)	0.3	0.3

The porosimetry analysis shows a decrease of the surface area of 13% after cycling confirming the retaining of the UTSA-16 structure.

S6.4 CO_2 adsorption isotherms at 298 K

Volumetric CO_2 adsorption were measured on fresh and cycled UTSA-16 samples by a volumetric instrument, Micromeritics ASAP 2020 system. UTSA-16 samples were previously activated over night at 363 K. The isotherms are reported in Figure S18. In the case of the cycled sample, the experimental data show a decrease of CO_2 adsorption of about 11% (3.9 mol kg^{-1}, blue line) when compared with the fresh powder (red lines). This result matches perfectly with the modest loss of surface area noted in Table S15, and further confirms the modest effect on UTSA-16 structure of the cycling in wet environment.
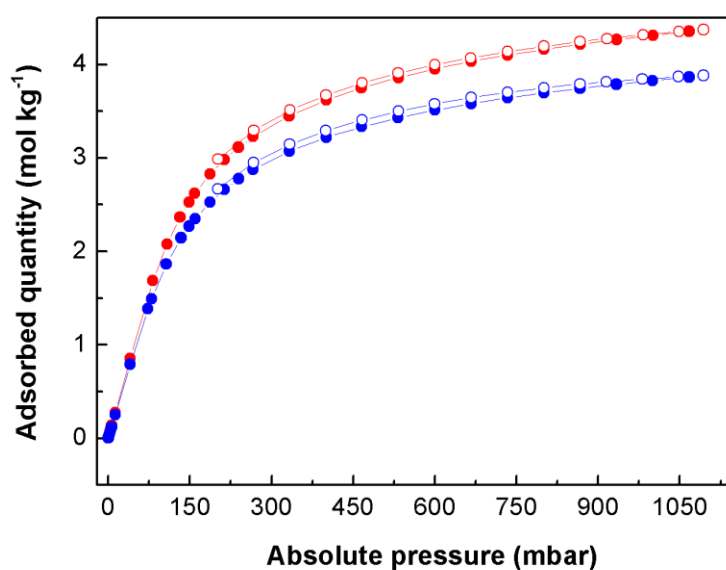
Figure S18 CO_2 adsorption on UTSA-16 particles after cycling. Adsorption isotherms at 298 K of CO_2 on a fresh (red) and on a cycled UTSA-16 (blue) samples. Full symbols refers to the adsorption branch; empty symbols refer to the desorption branch.

Bibliography

1.   Wang, Q. M.; Shen, D. M.; Bulow, M.; Lau, M. L.; Deng, S. G.; Fitch, F. R.; Lemcoff, N. O.; Semanscin, J., Metallo-Organic Molecular Sieve for Gas Separation and Purification. *Microporous Mesoporous Mat.* **2002,** *55* (2), 217-230.
2.   Al-Janabi, N.; Hill, P.; Torrente-Murciano, L.; Garforth, A.; Gorgojo, P.; Siperstein, F.; Fan, X. L., Mapping the Cu-btc Metal-Organic Framework (HKUST-1) Stability Envelope in the Presence of Water Vapour for CO_2 Adsorption from Flue Gases. *Chem. Eng. J.* **2015,** *281*, 669-677.
3.   Mason, J. A.; Sumida, K.; Herm, Z. R.; Krishna, R.; Long, J. R., Evaluating Metal-Organic Frameworks for Post-Combustion Carbon Dioxide Capture Via Temperature Swing Adsorption. *Energy Environ. Sci.* **2011,** *4* (8), 3030-3040.
4.   Stephenson, R. M.; Malanowski, S., Properties of Organic Compounds. In *Handbook of the Thermodynamics of Organic Compounds*, Springer, Ed. Amsterdam, Netherlands, **1987**, pp 1-471.
5.   Haynes, W. M., *Crc Handbook of Chemistry and Physics*. Boca Raton, Florida, **2003**; Vol. 84th.
6.   Simmons, J. M.; Wu, H.; Zhou, W.; Yildirim, T., Carbon Capture in Metal-Organic Frameworks-a Comparative Study. *Energy Environ. Sci.* **2011,** *4* (6), 2177-2185.
7.   Yang, Q. Y.; Xue, C. Y.; Zhong, C. L.; Chen, J. F., Molecular Simulation of Separation of CO_2 from Flue Gases in Cu-btc Metal-Organic Framework. *Aiche Journal* **2007,** *53* (11), 2832-2840.
8.   Dietzel, P. D. C.; Johnsen, R. E.; Fjellvag, H.; Bordiga, S.; Groppo, E.; Chavan, S.; Blom, R., Adsorption Properties and Structure of CO_2 Adsorbed on Open Coordination Sites of Metal-Organic Framework Ni_2(dhtp) from Gas Adsorption, IR Spectroscopy and X-Ray Diffraction. *Chem. Commun.* **2008,** (41), 5125-5127.
9.   Caskey, S. R.; Wong-Foy, A. G.; Matzger, A. J., Dramatic Tuning of Carbon Dioxide Uptake Via Metal Substitution in a Coordination Polymer with Cylindrical Pores. *J. Am. Chem. Soc.* **2008,** *130* (33), 10870-10871.
10.   Dietzel, P. D. C.; Besikiotis, V.; Blom, R., Application of Metal-Organic Frameworks with Coordinatively Unsaturated Metal Sites in Storage and Separation of Methane and Carbon Dioxide. *J. Mater. Chem.* **2009,** *19* (39), 7362-7370.
11.   Britt, D.; Furukawa, H.; Wang, B.; Glover, T. G.; Yaghi, O. M., Highly Efficient Separation of Carbon Dioxide by a Metal-Organic Framework Replete with Open Metal Sites. *Proc. Natl. Acad. Sci. U. S. A.* **2009,** *106* (49), 20637-20640.
12.   Chavan, S.; Bonino, F.; Vitillo, J. G.; Groppo, E.; Lamberti, C.; Dietzel, P. D. C.; Zecchina, A.; Bordiga, S., Response of Cpo-27-Ni Towards CO, N_2 and C_2h_4. *Phys. Chem. Chem. Phys.* **2009,** *11* (42), 9811-9822.
13.   Myers, A. L.; Prausnitz, J. M., Thermodynamics of Mixed-Gas Adsorption. *Aiche Journal* **1965,** *11* (1), 121-127.
14.   Simon, C. M.; Smit, B.; Haranczyk, M., Pyiast: Ideal Adsorbed Solution Theory (IAST) Python Package. *Comput. Phys. Commun.* **2016,** *200*, 364-380.

15.   Sumida, K.; Rogow, D. L.; Mason, J. A.; McDonald, T. M.; Bloch, E. D.; Herm, Z. R.; Bae, T. H.; Long, J. R., Carbon Dioxide Capture in Metal-Organic Frameworks. *Chem. Rev.* **2012,** *112* (2), 724-781.

16.   Cavenati, S.; Grande, C. A.; Rodrigues, A. E., Adsorption Equilibrium of Methane, Carbon Dioxide, and Nitrogen on Zeolite 13X at High Pressures. *J. Chem. Eng. Data* **2004,** *49* (4), 1095-1101.

17.   Belmabkhout, Y.; Pirngruber, G.; Jolimaitre, E.; Methivier, A., A Complete Experimental Approach for Synthesis Gas Separation Studies Using Static Gravimetric and Column Breakthrough Experiments. *Adsorption-Journal of the International Adsorption Society* **2007,** *13* (3-4), 341-349.

18.   Ruthven, D. M., *Principles of Adsorption and Adsorption Processes*. John Wiley & Sons: **1984**.

19.   Shen, C. Z.; Grande, C. A.; Li, P.; Yu, J. G.; Rodrigues, A. E., Adsorption Equilibria and Kinetics of CO2 and N-2 on Activated Carbon Beads. *Chem. Eng. J.* **2010,** *160* (2), 398-407.

20.   Delgado, J. A.; Agueda, V. I.; Uguina, M. A.; Sotelo, J. L.; Brea, P.; Grande, C. A., Adsorption and Diffusion of H_2/CO, CH_4, and CO_2 in Bpl Activated Carbon and 13X Zeolite: Evaluation of Performance in Pressure Swing Adsorption Hydrogen Purification by Simulation. *Ind. Eng. Chem. Res.* **2014,** *53* (40), 15414-15426.

21.   Xiang, S. C.; He, Y. B.; Zhang, Z. J.; Wu, H.; Zhou, W.; Krishna, R.; Chen, B. L., Microporous Metal-Organic Framework with Potential for Carbon Dioxide Capture at Ambient Conditions. *Nat. Commun.* **2012,** *3*, 953-962.

22.   de Jong, K. P., *Synthesis of Solid Catalysts*. John Wiley & Sons: **2009**; p 401.

23.   Masala, A.; Vitillo, J. G.; Bonino, F.; Manzoli, M.; Grande, C. A.; Bordiga, S., New Insights into UTSA-16. *Phys. Chem. Chem. Phys.* **2016,** *18* (1), 220-227.